## PAPER

# Highly efficient adsorbent design using a Cu-BTC/CuO/carbon fiber paper composite for high CH$_4$/N$_2$ selectivity†

Zhi-Guo Qu,[*a] Hui Wang[a] and Wen Zhang[*b]

A highly efficient adsorbent containing a Cu-BTC/CuO/CFP composite with a microporous copper benzene−1,3,5-tricarboxylate/CuO coating on a macroporous carbon fiber paper was designed *via* atomic layer deposition with the synthesis time of 6 h. The existing moderate CuO in Cu-BTC/CuO/CFP forms micropores between CuO and Cu-BTC and CuO and CFP to promote selectivity of CH$_4$/N$_2$. The effects of synthesis time and CuO content on the selectivity of CH$_4$/N$_2$ and effective thermal conductivity were experimentally investigated. The pressure drop and adsorption rate of the adsorption bed and temperature response of the desorption bed were numerically predicted. The selectivity of equimolar CH$_4$/N$_2$ for Cu-BTC/CuO/CFP (0.30 : 0.13 : 0.57) (6 h) is 2.15−2.65 times higher than that of pure Cu-BTC. The Cu-BTC/CuO/CFP material has higher effective thermal conductivity, lower pressure drop, higher adsorption rate, and better temperature uniformity compared to pure Cu-BTC powder in the adsorption bed.

## 1. Introduction

Methane (CH$_4$), which is the main component of shale gas, is an advantageous alternative to petroleum as a transportation fuel because of its increasing supply and potentially lower emission of greenhouse gases.[1] However, two major challenges are encountered in methane application. The density of CH$_4$ is relatively low under ambient conditions; thus, CH$_4$ requires densification in a storage tank. An adsorbent is usually placed in a tank to absorb CH$_4$ to enhance storage at low pressure. In addition, CH$_4$ is difficult to separate from mixture gases, such as CH$_4$/N$_2$ and CH$_4$/CO$_2$, because of the impurities (N$_2$ and CO$_2$) present during the production of shale gas.[2] Metal–organic frameworks (MOFs) are promising materials to overcome these two challenges related with CH$_4$ storage[3] and separation.[4] The well-known benefits of MOFs include adjustable chemical functionality, large surface area, fine-tunable pore structure, high selectivity, and high controllability.

Cu-BTC, as a typical MOF, is a promising candidate for CH$_4$ storage or gas separation.[5] Hulvey *et al.*[6] elucidated the mechanistic explanation for the high-uptake CH$_4$ adsorption capacity in Cu-BTC. The CH$_4$ uptake capacity is related to a small octahedral cage in its structure and is insensitive to primary adsorption sites. Hamon *et al.*[7] calculated the separation of CO$_2$/CH$_4$ and found that Cu-BTC shows a CO$_2$/CH$_4$ selectivity of ∼8. To further improve the gas adsorption capacity and selectivity of the Cu-BTC metal–organic framework, various modifications have been applied. Liu *et al.*[8] added 9% graphite oxide (GO) to Cu-BTC powder and found that Cu-BTC/GO exhibits about a 30% increase in CO$_2$ storage capacity. The enhancement in CO$_2$ storage capacity is due to the nanosized and well-dispersed Cu-BTC crystallites on the layers of GO. Policicchio *et al.*[9] investigated the adsorption capacity of Cu-BTC/aminated GO composites within the pressure range from 0 kPa to 15 000 kPa at ambient temperature. The modified GO with the highest nitrogen content exhibits 13.41 mmol g$^{-1}$ CO$_2$ adsorption at 298.15 K and 15 000 kPa. Petit *et al.*[10] tested the ammonia adsorption of Cu-based MOF/GO composites at room temperature under both dry and moist conditions and they found that the ammonia adsorption capacities on the composites were higher than those of the physically mixed components. They considered that the increased porosity and dispersive forces of graphene layers are responsible for the enhanced ammonia adsorption. Xu *et al.*[11] adopted an ultrafast synthetic method to prepare GO/Cu-BTC composites. They found that the CO$_2$/N$_2$ adsorption selectivity in 2GO/Cu-BTC is 1.8 times higher compared to that in the parent Cu-BTC. Wang *et al.*[12] reported a multi-scale porous composite adsorbent with a Cu-BTC coating on copper foam (Cu-BTC/CF) and found that the selectivity of CH$_4$/N$_2$ in 80 pores per linear inch Cu-BTC/CF is 1.41−2.95 times higher than that in pure Cu-BTC due to restriction in the growth of the Cu-BTC crystal.

[a] MOE Key Laboratory of Thermo-Fluid Science and Engineering, School of Energy and Power Engineering, Xi'an Jiaotong University, Xi'an, Shaanxi 710049, China. E-mail: zgqu@mail.xjtu.edu.cn; Fax: +86-029-82668543; Tel: +86-029-82668543

[b] School of Science, Xi'an Jiaotong University, Xi'an, Shaanxi 710049, China. E-mail: zhangwen@mail.xjtu.edu.cn

† Electronic supplementary information (ESI) available: Material characterization (*i.e.*, SEM images of the different samples at 3, 9, 18, 24 h and different component fractions of Cu-BTC/CuO/CFP, N$_2$ adsorption and desorption isotherms of the different samples, and the fitted parameters of the Langmuir–Freundlich (DSLF) model) information is available. See DOI: 10.1039/c6ra28124a

Although pure MOFs have shown compelling potential usages, their thermal transport properties impede their actual application because of low thermal conductivity. For example, the effective thermal conductivity of MOF-5 powder is just 0.091 W $(m^{-1} K^{-1})$[13] because of its high porosity (above 0.8) and high free volume. The low effective thermal conductivity of MOFs induces the adsorption heat to slowly transmit out of the adsorption bed. Wang et al.[14] found that the amount of $CO_2$ adsorption in the Cu-BTC powder decreases by 81.31% at 378.15 K compared to that at 298.15 K and 100 kPa. Mixing of highly heat-conductive materials into MOFs was carried out to achieve high effective thermal conductivity of MOF composite materials in the storage tank. For example, the effective thermal conductivity of MOF-5/natural graphite is nearly 6.5 times higher compared to that of pure Cu-BTC powder.[15] Carbon fiber paper (CFP) can be employed as a composite matrix to augment the thermal conductivity of the adsorption material and relieve the extreme temperature non-uniformity of pure MOFs. However, recently, the related CFP composite is majorly used in electrode materials for gas diffusion.[16] Zhang et al.[17] studied the effect of directly dispersing GO sheets onto the surface of individual carbon fibers on the interfacial properties of carbon fiber/epoxy composites. The results showed that the interfacial and tensile properties in the GO-modified carbon fiber composites are improved.

A highly efficient adsorbent should also possess a low pressure drop, high adsorption rate in the adsorption process, and long-term stability and regenerability during regeneration in the desorption process. Silva et al.[18] reported $H_2$ purification from mixtures that contain $CO_2$, $CH_4$, and $N_2$ with Cu-BTC particles as the adsorbent and found that the pressure drop can reach up to 250 kPa. Moreover, a high temperature (above 373.15 K) in the adsorption bed under vacuum conditions ($10^{-5}$ kPa) or inert gas purge is required for the desorption process. The minimum temperature difference between the heating surface and outside boundary and heating time duration are the two key factors in gauging regenerability. Liu et al.[19] found that the remaining 6% residual $CO_2$ in the Ni/DOBDC adsorption bed should be removed at 523.15 K with a helium purge. Wurzbacher et al.[20] removed the adsorbed $CO_2$ in an amine-functionalized nanofibrillated cellulose sorbent material within the temperature range of 293.15–368.15 K and under vacuum at 6.2 kPa. The group found that more than 90% of the captured $CO_2$ can be recovered under the abovementioned conditions.

As abovementioned, it is practical to form a high heat thermal-conductive adsorbent to replace pure MOFs. High selectivity, low pressure drop, high adsorption rate, long-term stability, and easy regenerability are all the key elements for an efficient adsorbent design. However, few studies have been found to involve all the abovementioned elements. To the best of our knowledge, MOF adsorbents supported on CFP skeletons have not been investigated, especially for binary mixtures formed on CFP. In the present study, the MOF adsorbent was coated on the skeletons of CFP to form a multi-level porous adsorbent structure to improve gas selectivity and effective thermal conductivity in the adsorption bed. Cu-BTC/CuO/CFP

and Cu-BTC/CFP were synthesized by controlling the synthesis time to further investigate the effects of CuO on gas adsorption and separation. The adsorption capacity ($N_2$ and $CH_4$) and selectivity of $CH_4/N_2$ in Cu-BTC/CFP at different synthesis times and in different component fractions of Cu-BTC/CuO/CFP were experimentally investigated. The effective thermal conductivities of different component fractions of Cu-BTC/CuO/CFP were also experimentally studied. Moreover, the pressure drop, adsorption rate, and temperature response of the adsorption bed were simulated.

## 2. Material preparation and characterization

Fig. 1 shows the synthetic route for the Cu-BTC/CuO composite in CFP. Prior to the synthetic process, several basic materials were prepared. CFP with a 0.019 cm thickness was obtained from Japan Toray (TGP-060). Inside the CFP, the carbon fibers and carbon sheets were interwoven. Trimesic acid (1,3,5-benzenetricarboxylic acid, $H_3BTC$), copper acetate ($Cu(OAc)_2$), and copper nitrate ($Cu(NO_3)_2$) were obtained from Sigma-Aldrich. Hydrogen dioxide ($H_2O_2$, 30%) was obtained from Sinopharm Chemical Reagent. All the reagents were of analytical reagent grade.

The synthesis of Cu-BTC/CuO/CFP is based on atomic layer deposition (ALD). Two major stages of pretreatment and synthesis were used in the process of synthesizing Cu-BTC/CuO/CFP. In the pretreatment stage, a sheet of CFP (2.5 cm × 3.0 cm) was dipped in a 25 mL of hydrogen dioxide ($H_2O_2$, 30%) and ultrasonicated for 2 h every 10 h six times at 50 °C. Then, the CFP was removed and thoroughly washed with deionized water. The modified CFP was dried in an oven at 323.15 K for 24 h. In the synthesis stage, 1.0 mM copper acetate aqueous solution ($Cu(OAc)_2 \cdot H_2O$) and 0.2 mM $H_3BTC$ ethanolic solution were separately prepared to supply $Cu^{2+}$ and ligands. The modified CFP was immersed in the $Cu^{2+}$ source solution for 20 min and then in an $H_3BTC$ solution reaction vessel for 20 min at 323.15 K to grow seeds. The modified CFP with seeds was thoroughly rinsed with ethanol to remove excess reagent on the CFP surface. The abovementioned operation from immersion in $Cu^{2+}$ solution to rinsing was repeated for 10 cycles. After this, the seeded CFP was dried at 323.15 K. Isovolumetric $Cu(NO_3)_2 \cdot 3H_2O$ (0.1226 mol $L^{-1}$) and an $H_3BTC$ (0.08 mol $L^{-1}$) ethanolic solution were mixed and stirred for 30 min. Then, the mixed solution was transferred to a 100 mL autoclave. The seeded CFP was vertically inserted into the autoclave, and then the autoclave was capped and heated at 368.15 K for different times (3, 6, 9, 18, and 24 h). The appearance of Cu-BTC or Cu-BTC/CuO seeds is dependent on the crystal growth time (3, 6, 9, 18, and 24 h) because of the existence of a competitive relationship between Cu-BTC and the CuO coating on CFP. Small Cu-BTC crystals appeared in CFP at the synthesis time of 3 h. The acid–base reaction is as follows:

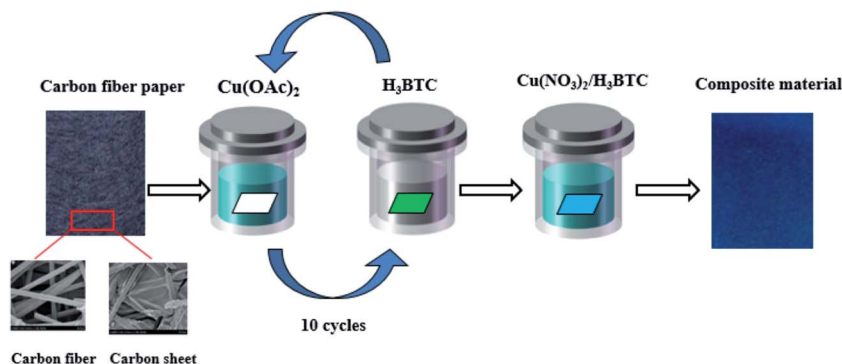$$3Cu^{2+} + 2BTC^{3-} = Cu_3BTC_2 \qquad (1)$$
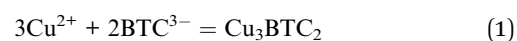
Fig. 1  Schematic of the synthesis route for Cu-BTC in CFP.

When the synthesis time increased from 3 to 6 h, the Cu-BTC crystals were gradually enlarged, as shown in Fig. S1(a)† and 2(a), because the solution at this stage could provide enough copper ions to form large Cu-BTC crystals and $Cu(OH)_2$ starts to appear in CFP. Although the existence of $Cu(OH)_2$ cannot be directly observed *via* scanning electron microscopy (SEM), it can be indirectly inferred from the existing CuO because $Cu(OH)_2$ can be easily changed into CuO when the sample is dried in an oven (323.15 K) for the property test. The existing CuO was validated *via* transmission electron microscopy (TEM). Moreover, $Cu(OH)_2$ that appears in the synthesis of Cu-BTC has also been demonstrated by Majano *et al.*[21] and Jaggi *et al.*[22] The solution can offer enough $Cu^{2+}$ to react as follows:

$$Cu^{2+} + 2OH^{2-} = Cu(OH)_2 \qquad (2)$$

$$3Cu^{2+} + 2BTC^{3-} = Cu_3BTC_2 \qquad (3)$$
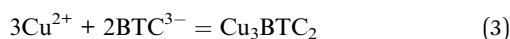
When the synthesis time increased from 6 to 9 h, the average size of the Cu-BTC crystals decreased, as shown in Fig. S1(b).† The reason is that copper ions in the fluid were exhausted, such that copper ions in $Cu(OH)_2$ and parts of small Cu-BTC crystals started to dissolve to provide copper ions for the formation of new Cu-BTC crystals. This process is expressed as a simple acid–base reaction:

$$3Cu(OH)_2 + 6H^+ + 2BTC^{3-} = Cu_3BTC_2 + 6H_2O \qquad (4)$$
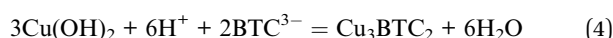
This conversion strongly occurs inside the $Cu(OH)_2$ aggregates and is accompanied by recrystallization. $Cu(OH)_2$ consists of chains of distorted octahedra organized as corrugated layers. The Cu–Cu distance between two layer ranges from 0.295–0.344 nm, which is fitted for the diffusion of the linker molecule to form Cu-BTC, as described by Jaggi *et al.*[22] When the synthesis time was increased to 18 h, the average size of the Cu-BTC crystals gradually increased, as shown in Fig. S1(c).† This illustrates that the newly formed Cu-BTC crystals with a bigger size, especially in the carbon fibers, develop and parts of the small Cu-BTC crystals completely dissolve. When the synthesis time was 24 h, the average size of the Cu-BTC crystals continuously increased, and the size of the Cu-BTC crystals also

became homogeneous, as shown in Fig. S1(d),† because the newly formed Cu-BTC crystals with a bigger size replace the dissolved small sized Cu-BTC crystals. After the reaction, the composite was taken out and was successively rinsed three times with dimethylformamide and deionized water. Finally, the sample was dried in an oven (323.15 K) and stored for testing. The final adsorption capacity is strongly related to synthesis time.

The microtopography of the sample was visualized using SEM (HITACHI S-4800, Japan). The sample was coated with a thin layer of gold to avoid charging prior to scanning, and scanning was conducted to demonstrate microtopography at the typical synthesis times of 3, 9, 18, and 24 h. Scanning was further performed *via* TEM. TEM images were obtained using a JEM-2000EX transmission electron microscope to demonstrate the components of the composite. The images obtained *via* SEM and TEM at the typical synthesis time of 6 h are shown in Fig. 2. The CuO and Cu-BTC structures can also be identified in the TEM image shown in Fig. 2(b). The measured interplanar distance is $d_{111} = 0.232$ nm, which is consistent with the interplanar distance for CuO.[23] The measured interplanar
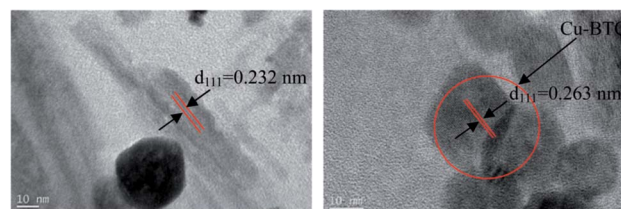


(a)  TEM of the synthesized Cu–BTC/CuO/CFP.
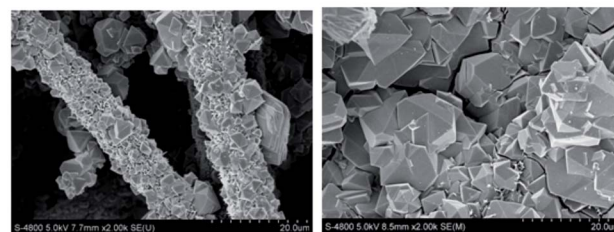


(b)  SEM of the synthesized Cu–BTC/CuO/CFP

Fig. 2  TEM and SEM images of the synthesized Cu-BTC/CuO/CFP.

Table 1 Properties of different samples

| Sample | BET ($m^2 g^{-1}$) | Loading (wt%) |
|---|---|---|
| Carbon fiber paper | 70.0 | — |
| CuO | 53.2 | — |
| Cu-BTC | 1504.9 | — |
| 3 h | 174.2 | 6.14 |
| Cu-BTC/CuO/CFP, (0.30 : 0.13 : 0.57) (6 h) | 500.6 | 42.58 |
| Cu-BTC/CuO/CFP, (0.28 : 0.11 : 0.61) (6 h) | 452.1 | 37.40 |
| Cu-BTC/CuO/CFP, (0.09 : 0.21 : 0.70) (6 h) | 180.3 | 30.45 |
| 9 h | 422.1 | 42.42 |
| 18 h | 306.8 | 36.76 |
| 24 h | 367.3 | 43.88 |

distance is $d_{111} = 0.263$ nm, which is consistent with the interplanar distance for Cu-BTC.[24] Thus, these results prove that the Cu-BTC/CuO/CFP composite is obtained at the synthesis time of 6 h. The Cu-BTC crystals, as shown in Fig. 2(b), are heterogeneously distributed in the carbon sheet and glittery carbon fiber; thus, it seems that the Cu-BTC crystals stack in the carbon sheet and glittery carbon fiber. To clearly display the Cu-BTC and CuO coating on the carbon sheet and glittery carbon fiber, the SEM image during the process of growing seeds is shown in Fig. S2(a)† and an SEM image of the CuO coating on CFP is shown in Fig. S2(b).† As shown in Fig. S2(a) and (b),† both the Cu-BTC crystals and CuO directly coat CFP. Carboxyl and hydroxyl groups can exist in CFP after CFP is modified by hydrogen peroxide ($H_2O_2$, 30%). Thus, Cu-BTC and CuO can embed in the carbon sheet and glittery carbon fibers. This is similar to the Cu-BTC crystals coating in aminated GO through the carboxyl and hydroxy groups.[25] The SEM results of the composite at other synthesis times of 3, 9, 18, and 24 h are provided in Fig. S1 in the (ESI†). Only Cu-BTC was found to exist in CFP at these times.

The CuO component fraction in Cu-BTC/CuO/CFP (6 h) can be further controlled by adjusting the amount of $H_3BTC$. The corresponding components of Cu-BTC/CuO/CFP (6 h) can be calculated via the BET method, as suggested by Chen et al.[26] Three typical component fractions of (0.30 : 0.13 : 0.57) (0.28 : 0.11 : 0.61) and (0.09 : 0.21 : 0.70) were obtained. Note that the fraction of (0.30 : 0.13 : 0.57) in Cu-BTC/CuO/CFP (6 h) was regarded as the reference fraction.

To obtain the Brunauer–Emmett–Teller (BET) values of the Cu-BTC/CFP composite at different synthesis times (3, 9, 18, and 24 h) and Cu-BTC/CuO/CFP (6 h) with three fractions: Cu-BTC, CuO, and CFP, $N_2$ adsorption–desorption isotherms at 77 K were obtained and are provided in Fig. S3 and S4,† respectively. The BET values of CFP, CuO, Cu-BTC, Cu-BTC/CFP (3, 9, 18, and 24 h), and Cu-BTC/CuO/CFP (6 h) with three fractions are shown in Table 1. The pore structure parameters of CFP, CuO, Cu-BTC, Cu-BTC/CFP (3, 9, 18, and 24 h), and Cu-BTC/CuO/CFP (6 h) with three fractions are shown in Table 2. As shown in Tables 1 and 2, the BET and pore volume of Cu-BTC is the highest among all the materials.

The effective thermal conductivity of the samples was measured using the $3 - \omega$ method based on a transient hot wire method (TC3000E, Xi'an Xiaxi), which is mainly used for testing films. The accuracy of this instrument is 2% at room temperature and standard pressure (298.15 K and 101.1 kPa).[27] The porosity, heat capacity, and density of pure Cu-BTC and the Cu-BTC/CuO/CFP (0.30 : 0.13 : 0.57) (6 h) composite are summarized in Table 3. The abovementioned properties for pure Cu-BTC are based on the study reported by Plaza et al.,[28] and the values for Cu-BTC/CuO/CFP (0.30 : 0.13 : 0.57) (6 h) were mainly obtained from the present experiment. Solid heat capacity was tested by a Calvet calorimeter (C80, France) and the porosity of Cu-BTC/CuO/CFP (0.30 : 0.13 : 0.57) (6 h) was tested by mercury porosimetry. The permeability of Cu-BTC and Cu-BTC/CuO/CFP (6 h) was tested by a permeability detector (Miner Searle Bate,

Table 2 Pore structure parameters of different samples[a]

| Material | Pore volume ($cm^3 g^{-1}$) | | | | | |
|---|---|---|---|---|---|---|
| | $V_{total}$ | Newly formed | $V_{meso}$ | Newly formed | $V_{micro}$ | Newly formed |
| Carbon fiber paper | 0.098 | — | 0.098 | — | 0.000 | — |
| CuO | 0.104 | — | 0.104 | — | 0.000 | — |
| Cu-BTC | 0.950 | — | 0.485 | — | 0.465 | — |
| 3 h | 0.176 | 0.055 | 0.176 | 0.055 | 0.000 | 0 |
| Cu-BTC/CuO/CFP, (0.30 : 0.13 : 0.57) (6 h) | 0.482 | 0.134 | 0.244 | 0.035 | 0.238 | 0.099 |
| Cu-BTC/CuO/CFP, (0.28 : 0.11 : 0.61) (6 h) | 0.466 | 0.129 | 0.246 | 0.039 | 0.220 | 0.090 |
| Cu-BTC/CuO/CFP, (0.09 : 0.21 : 0.70) (6 h) | 0.204 | 0.029 | 0.154 | 0.020 | 0.05 | 0.009 |
| 9 h | 0.477 | 0.021 | 0.273 | 0.012 | 0.204 | 0.009 |
| 18 h | 0.465 | 0.118 | 0.259 | 0.084 | 0.206 | 0.034 |
| 24 h | 0.481 | 0.008 | 0.275 | 0.007 | 0.206 | 0.001 |

[a] $V_{total}$: total pore volume when pressure is $P/P_0 = 0.995$; $V_{micro}$: micro-pore volume calculated using the t-plot method; and $V_{meso}$: meso-pore volume calculated by $V_{total} - V_{micro}$ according to Xu et al.[11] The newly formed pore volumes were calculated using the BET method.[26]

**Table 3** General physical properties of Cu-BTC, Cu-BTC/CuO/CFP (0.30 : 0.13 : 0.57) (6 h), and $CH_4$

| Property | Cu-BTC[28] | Cu-BTC/CuO/CFP (0.30 : 0.13 : 0.57) (6 h) | $CH_4$ |
|---|---|---|---|
| Porosity | 0.41 | 0.78 | — |
| Solid heat capacity (J $kg^{-1}$ $K^{-1}$) | 1456 | 937.9 | — |
| Solid density (kg $m^{-3}$) | 1379 | 2000 | — |
| $K_m$ internal mass transfer coefficient (1/s) | 0.62 | 0.62 | — |
| Permeability ($m^2$) | $1.188 \times 10^{-8}$ | $1.9 \times 10^{-8}$ | — |
| Density of $CH_4$ (kg $m^{-3}$) | — | — | 0.717 |
| Molecular weight | — | — | 16.0428 |
| Viscosity (Pa s) | — | — | $1.0806 \times 10^{-5}$ |
| Effective thermal conductivity (W $m^{-1}$ $K^{-1}$) | 0.0678 | 1.196 | — |

Beijing). Gas was fed through pure Cu-BTC and Cu-BTC/CuO/CFP at a fixed flow rate and the resultant pressure drop was measured. The permeability ($K$) was obtained by combining the modified Darcy's law with the tested pressure drop.[29] Evidently, the porosity of Cu-BTC/CuO/CFP (0.30 : 0.13 : 0.57) (6 h) is 0.78, which is higher than that of pure Cu-BTC powder.

# 3. Model of pressure drop and adsorption rate and regenerability

The pressure drop and adsorption rate in the process of adsorption are the two keys to judge the efficiency of the adsorption bed. As shown in Fig. 3(a), a typical adsorption bed filled with pure Cu-BTC particles or Cu-BTC/CuO/CFP (0.30 : 0.13 : 0.57) (6 h) was used to predict the pressure drop and adsorption rate. The length of the reduced model is 0.1 m ($X = R = 0.1$ m) at both the axial and radial distances. The bed adsorption column can be reduced as a two-dimensional model, as shown in Fig. 3(b). The adsorption bed is uniformly packed, and the macro scale mass conservation equation can be expressed as follows:

$$\varepsilon \frac{\partial(\rho_g)}{\partial t} + \frac{1}{r}\frac{\partial(r\rho_g v_r)}{\partial r} + \frac{\partial(\rho_g u_x)}{\partial x} + (1-\varepsilon)\rho_s\frac{\partial N}{\partial t} = 0 \quad (5)$$

where $\varepsilon$ is the porosity of the adsorption bed, $\rho_g$ is the density of adsorbate, $u_x$ and $v_r$ are the velocities of the $x$ and $r$ axis, respectively, $\rho_s$ is the density of the adsorbent, and $N$ is the amount of adsorption at $t$ time. The linear driving force (LDF) was used to describe the adsorption rate as follows:

$$\frac{\partial N}{\partial t} = k_m(N_\infty - N) \quad (6)$$

Where $N_\infty$ is the saturation amount of adsorption, and $k_m$ is the internal mass transfer coefficient. The Darcy–Brinkman formulation that considers the viscous effects was used:

*x*-Momentum equation:

$$\frac{\rho_g}{\varepsilon}\left(\frac{\partial u_z}{\partial t}\right) + \frac{\rho_g}{\varepsilon^2}\left(u_x\frac{\partial u_x}{\partial x} + v_r\frac{\partial u_x}{\partial x}\right) = -\frac{\partial p}{\partial x}$$
$$+ \mu_g\left[\frac{1}{r}\frac{\partial}{\partial r}\left(\frac{\partial u_x}{\partial r}\right) + \frac{\partial^2 u_x}{\partial x^2}\right] - \frac{\mu_g}{K}u_x \quad (7)$$

*r*-Momentum equation:

$$\frac{\rho_g}{\varepsilon}\left(\frac{\partial v_r}{\partial t}\right) + \frac{\rho_g}{\varepsilon^2}\left(v_r\frac{\partial v_r}{\partial r} + u_x\frac{\partial v_r}{\partial r}\right) = -\frac{\partial p}{\partial r}$$
$$+ \mu_g\left[\frac{1}{r}\frac{\partial}{\partial r}\left(\frac{\partial v_r}{\partial r}\right) + \frac{\partial^2 v_r}{\partial x^2}\right] - \frac{\mu_g}{K}v_r \quad (8)$$

where $p$ is the pressure, $\mu_g$ is the gas velocity, and $K$ is the permeability. The values of the abovementioned parameters are shown in Table 3.

Initial condition:

$$p(t, x, r)|_{t=0} = 101 \text{ kPa} \quad (9)$$

Boundary conditions:

$$u(t,x,r)|_{x=0} = u_{in}; \quad v(t,x,r)|_{x=0} = 0;$$
$$\frac{\partial u(t,x,r)}{\partial r}\Big|_{x=X} = \frac{\partial v(t,x,r)}{\partial r}\Big|_{x=X} = 0 \quad (10a)$$

$$\frac{\partial u(t,x,r)}{\partial y}\Big|_{r=0} = v(t,x,r)|_{r=0} = 0; \quad u(t,x,r)|_{r=R} = v(t,x,r)|_{r=R} = 0 \quad (10b)$$

The governing equations were discretized using the IDEAL algorithm[30] with a staggered grid system of $100 \times 100$. The iteration at the present time layer was considered convergent if the maximum relative residuals of the mass and momentum equations were less than $10^{-7}$.

Desorption is usually required for the regeneration of the adsorption bed. Desorption conditions include the lowest temperature in the adsorption bed of over 373.15 K under vacuum (low $1.0 \times 10^{-5}$ kPa). Fig. 3(c) shows a typical bed adsorption column containing the adsorbent [Cu-BTC or Cu-BTC/CuO/CFP (0.30 : 0.13 : 0.57) (6 h)] and a cylindrical heating rod. The cylindrical heating rod in the center of the adsorption bed supplies a constant heat flux during desorption. The length of the reduced model is 0.1 m ($X = R = 0.1$ m) at both the axial and radial distances. The bed adsorption column can be reduced as a two-dimensional model, as shown in Fig. 3(d). The governing equations are as follows:

$$(1-\varepsilon)\rho_s C_p\frac{\partial T_s}{\partial t} = k_{eff}\left[\frac{\partial^2 T_s}{\partial x^2} + \frac{1}{r}\frac{\partial}{\partial r}\left(\frac{\partial T_s}{\partial r}\right)\right] + q\Delta H \quad (11)$$
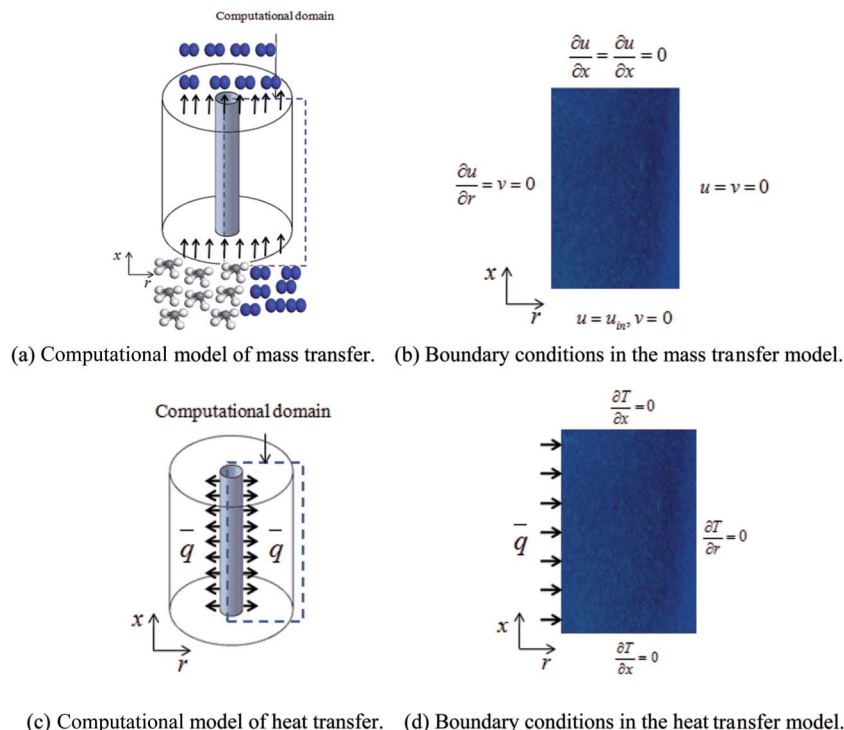
(a) Computational model of mass transfer.   (b) Boundary conditions in the mass transfer model.

(c) Computational model of heat transfer.   (d) Boundary conditions in the heat transfer model.

**Fig. 3**   Model of the adsorption bed.

Initial condition:

$$T_s(t, r, x)|_{t=0} = 298.15 \qquad (12)$$

Boundary conditions:

$$\bar{q}(t,r,x)|_{r=0} = 100 \text{ W m}^{-2}; \quad \frac{\partial T_s(t,r,x)}{\partial x}\Big|_{r=R} = 0 \qquad (13a)$$

$$\frac{\partial T_s(t,r,x)}{\partial r}\Big|_{x=0} = 0; \quad \frac{\partial T_s(t,r,x)}{\partial r}\Big|_{x=X} = 0 \qquad (13b)$$

where $\bar{q}$, $\rho_s$, $C_p$, $T_s$, $x$, $r$, and $t$ are the heat flux, solid density, heat capacity, solid temperature (K), axial and radial distances, and time, respectively. The corresponding values are also shown in Table 3. $q$ is the amount of adsorption that can be ignored under vacuum conditions (low $1.0 \times 10^{-5}$ kPa) for low 0.1% residual adsorbed gas under vacuum. $\Delta H$ is the isosteric heat of adsorption (kJ mol$^{-1}$) and $k_{eff}$ is the effective thermal conductivity of the adsorption bed. Without considering the gaseous phase under vacuum, the effective thermal conductivity of the adsorption bed can be reduced as follows:

$$k_{eff} = (1 - \varepsilon)k_s \qquad (14)$$

The governing equations were discretized using a finite volume method with a staggered grid system of $100 \times 100$.

## 4.   Results and discussion

### 4.1.   General adsorption and separation characteristics

Fig. 4(a) and (b) show the isotherms of $N_2$ and $CH_4$ in pure Cu-BTC, CFP, Cu-BTC/CuO/CFP (0.30 : 0.13 : 0.57) (6 h), and Cu-

BTC/CFP at different synthesis times (3, 9, 18, and 24 h) with pressure ranging from 0 to 100 kPa at 273.15 K. The $N_2$ and $CH_4$ uptakes for all the materials increased with an increase in pressure, except for CFP. The adsorption amount for Cu-BTC is the highest and that for CFP, is the lowest among the seven materials at the same pressure. For example, the $N_2$ and $CH_4$ adsorption amount in Cu-BTC/CuO/CFP (0.30 : 0.13 : 0.57) (6 h) is 35.97–37.33% and 77.72–83.32% lower compared to that in pure Cu-BTC, respectively. The $N_2$ and $CH_4$ adsorption amount in Cu-BTC/CuO/CFP (0.30 : 0.13 : 0.57) (6 h) and Cu-BTC/CFP at different synthesis times (3, 9, 18, and 24 h) first increased with an increase in synthesis time, and then continuously decreased with the increasing synthesis time. The $N_2$ and $CH_4$ adsorption amount reached maximum at the synthesis time of 6 h. Since the $N_2$ and $CH_4$ adsorption amounts in Cu-BTC/CuO/CFP (0.30 : 0.13 : 0.57) (6 h) and Cu-BTC/CFP at different synthesis times (3, 9, 18, and 24 h) are different compared to those of pure Cu-BTC, the selectivity of $CH_4/N_2$ in these composites will be also different from that in pure Cu-BTC.

The selectivity of $CH_4/N_2$ in the Cu-BTC/CFP composite at different synthesis times (3, 9, 18, 6 and 24 h), Cu-BTC, and CFP was investigated by the ideal adsorption solution theory (IAST).[31] The IAST method has been successfully demonstrated in the selectivity of $CO_2/CH_4$ in GrO/Cu-BTC.[32] The mixture adsorption equilibrium in the IAST model is predicted on the basis of a single-component adsorption isotherm. To start with the IAST method, the single gas component adsorption isotherm should be obtained first. The veracity of the fitted single component adsorption isotherm model is key for the IAST model. There are some simple adsorption isotherm
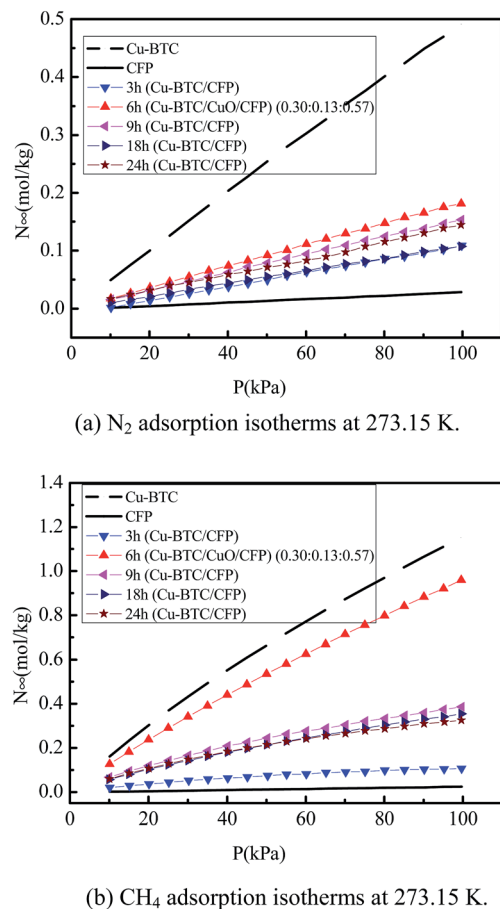
(a) $N_2$ adsorption isotherms at 273.15 K.



(b) $CH_4$ adsorption isotherms at 273.15 K.

**Fig. 4** $N_2$ and $CH_4$ adsorption isotherms at different synthesis times.

models such as the Langmuir model,[33] Toth isotherm model,[34] and the Toth equation[35] that are used to fit the experimental data. However, these models poorly fit in the low-pressure region because they do not consider metal sites.[36] The dual-site Langmuir–Freundlich (DSLF) model overcomes the above-mentioned shortcoming because the DSLF model assumes two adsorption sites of the open metal site and pore adsorption site. The DSLF model is particularly suitable for Cu-BTC, which has an obvious open metal site. The DSLF model has been widely used for $CO_2$ adsorption in GrO/Cu-BTC,[11] $CH_4$ adsorption in GrO/Cu-BTC,[32] and $CO_2$ adsorption in Cu-BTC/CF.[12] Therefore, the DSLF model was adopted and correlation coefficients of up to 0.999 were obtained, as shown in Table S1 in the ESI,† indicating that the DSLF model was accurately applied to fit the experimental isotherm. The fit parameters and the corresponding confidence intervals for the DSLF model are also presented in Table S1.†

The selectivity of $CH_4/N_2$ is dependent on the components of the composite that are affected by the synthesis time. Fig. 5(a) shows the selectivity of equimolar $CH_4/N_2$ at different synthesis times (3, 6, 9, 18, 6 and 24 h) within the pressure range of 0–100 kPa and 273.15 K. The selectivity of pure Cu-BTC and CFP is chosen for basic comparison. The selectivity of equimolar $CH_4/N_2$ in CFP retains a nearly constant value of 0.7 with an increase in pressure. The selectivity of equimolar $CH_4/N_2$ in pure Cu-BTC

and Cu-BTC/CFP (3, 9, 18, and 24 h) gradually decreased with an increase in pressure. The selectivity of equimolar $CH_4/N_2$ in Cu-BTC/CuO/CFP (0.30 : 0.13 : 0.57) (6 h) slowly decreased within the pressure range from 0 kPa to 50 kPa. This decrease trend is attributed to the fact that the micropores are blocked with $CH_4$ and $N_2$ molecules, as indicated by Li et al.[37] and Kim et al.[38] However, the selectivity gradually increased when the pressure continued to increase from 50 kPa to 100 kPa. This increase trend results from the fact that the $CH_4$ molecules go through the stoppage micropores because of the existing flexibility in the Cu-BTC crystal, as described by Zhao et al.[39] and Nazarian et al.[40] This phenomenon is similar to the process of $CO_2$ adsorption in MIL-53(Gr).[41]
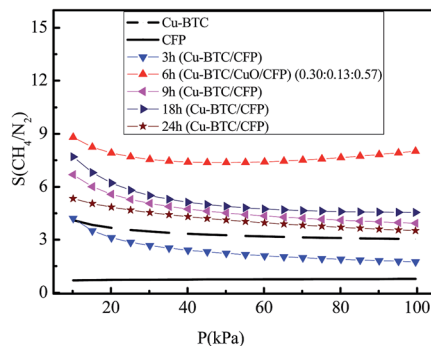
The selectivity of equimolar $CH_4/N_2$ in Cu-BTC/CFP (9, 18, and 24 h) is higher than that of pure Cu-BTC powder. These findings are attributed to two aspects, as shown in Fig. 5(b). First, certain smaller incomplete micropores (A) between the Cu-BTC crystals were formed because the growth of the Cu-BTC crystal was restrained by CFP during the synthesis. Second, micropores (B) were formed between Cu-BTC and CFP, as demonstrated in Table 2. The newly formed micropores and incomplete micropores adsorb $CH_4$ more easily compared to $N_2$, as described by Zhou et al.[42] and Policicchio et al.,[9] because the Cu-BTC crystals have COOH-terminated and OH-terminated surfaces.[43,44] Note that the selectivity of equimolar $CH_4/N_2$ in Cu-BTC/CFP (3 h) is even lower than that of pure Cu-BTC because the amount of Cu-BTC loading in CFP is small (6.14%).

At the same pressure, the selectivity of equimolar $CH_4/N_2$ decreases in the order of Cu-BTC/CuO/CFP (6 h), Cu-BTC/CFP (18 h), Cu-BTC/CFP (9 h), Cu-BTC/CFP (24 h), pure Cu-BTC, and Cu-BTC/CFP (3 h); for example, for Cu-BTC/CuO/CFP (0.30 : 0.13 : 0.57) (6 h), it is 7.37–8.81, which is 2.15–2.65 times higher than that of pure Cu-BTC powder. For Cu-BTC/ CuO/CFP (0.30 : 0.13 : 0.57) (6 h), selectivity is even higher than that in many other reported MOFs at 100 kPa,[45–49] as shown in Table 4. The superior selectivity of Cu-BTC/CuO/CFP (0.30 : 0.13 : 0.57) (6 h) is attributed to the existence of CuO in Cu-BTC/CFP, as shown in Fig. 2. The superiority of Cu-BTC/ CuO/CFP (0.30 : 0.13 : 0.57) (6 h) over pure Cu-BTC is ascribed to two reasons, as shown in Fig. 5(c). First, CuO provides new small specific micropores between Cu-BTC and CuO (B) and CuO and CFP (C), except for the formed micropores between Cu-BTC and CFP (D), to easily adsorb $CH_4$, as demonstrated in Table 2. Second, certain smaller incomplete micropores (A) in the Cu-BTC crystals are also formed and result in synergistic features that are beneficial for $CH_4$ adsorption.

### 4.2. Component fraction on the adsorption and selectivity of $CH_4/N_2$

The $CH_4$ and $N_2$ adsorption for three Cu-BTC/CuO/CFP (6 h) composites with component fractions of (0.30 : 0.13 : 0.57), (0.28 : 0.11 : 0.61), and (0.09 : 0.21 : 0.70) were investigated at pressures ranging from 0 to 100 kPa at 273.15 K, and the corresponding results are shown in Fig. 6(a) and (b). The $N_2$ and $CH_4$ adsorption capacities of the composites follow the order Cu-BTC/CuO/CFP (0.30 : 0.13 : 0.57) > Cu-BTC/CuO/CFP
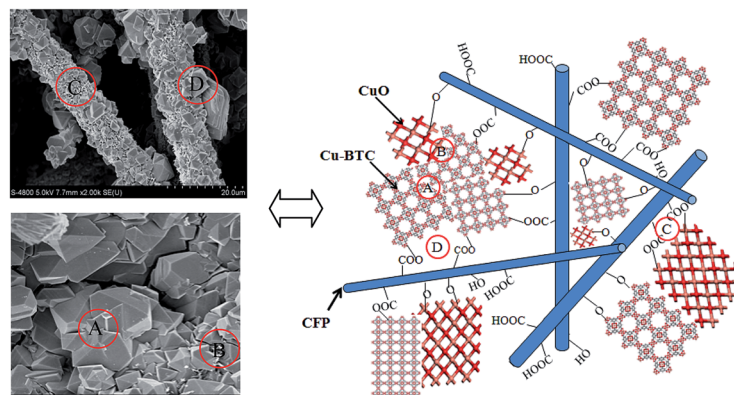
(a) Selectivity of an equimolar $CH_4/N_2$ mixture at different synthesis times.
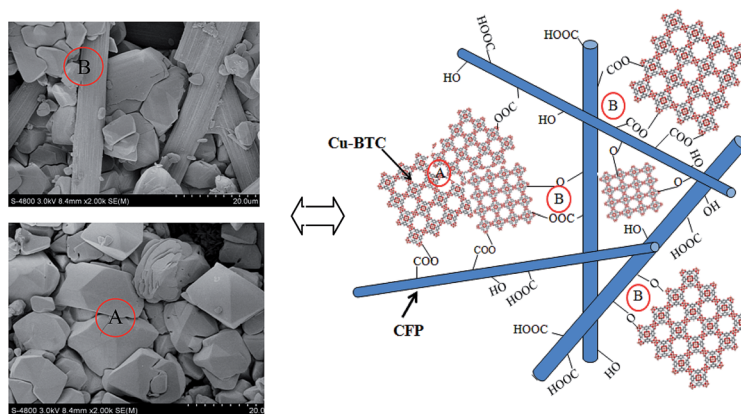


(b) Schematic of the Cu-BTC/CFP composite structure and SEM surface topography image of

Cu-BTC/CFP (A: incomplete micropores and B: micropores).



(c) The schematic of the Cu-BTC/CuO/CFP composite structure and SEM surface topography image of

Cu-BTC/CuO/CFP (6 h) (A : incomplete micropores; B: new micropores between Cu-BTC and CuO; C:

new micropores between CuO and CFP; and D: new micropores between Cu-BTC and CFP).

**Fig. 5** Selectivity of equimolar $CH_4/N_2$ at different synthesis times with the adsorption mechanism.

(0.28 : 0.11 : 0.61) > Cu-BTC/CuO/CFP (0.09 : 0.21 : 0.70). This illustrates that the adsorption capacity decreases with a decrease in Cu-BTC.
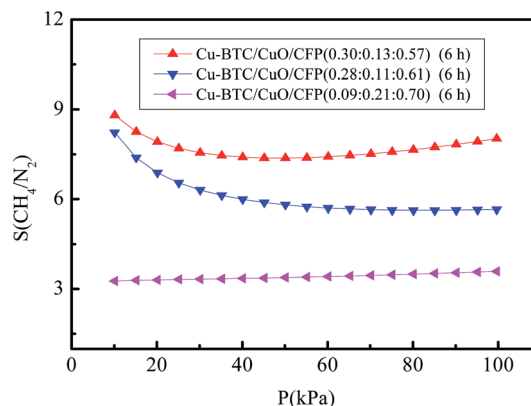
Fig. 7 shows the selectivity of equimolar $CH_4/N_2$ in Cu-BTC/CuO/CFP at the three component fractions of (0.30 : 0.13 : 0.57), (0.28 : 0.11 : 0.61), and (0.09 : 0.21 : 0.70) with pressures in the

**Table 4** Selectivity of $CH_4/N_2$ at 100 kPa on different adsorbents

| Adsorbent | Selectivity | Temperature (K) | Reference |
|---|---|---|---|
| Cu-BTC | 3.59 | 273.15 | This work |
| Cu-BTC/CFP (18 h) | 4.54 | 273.15 | This work |
| Cu-BTC/CuO/CFP, (0.30 : 0.13 : 0.57) (6 h) | 8.02 | 273.15 | This work |
| Cu-BTC | 3 | 298 | Liu *et al.*[45] |
| MIL-47 (V) | 5 | 298 | Liu *et al.*[45] |
| ZIF-69 | 3.1 | 298 | Liu *et al.*[46] |
| ZIF-68 | 3.7 | 298 | Liu *et al.*[46] |
| IRMOF-1 | 2 | 298 | Liu *et al.*[46] |
| $[Ni_3(HCOO)_6]$ | 6.6 | 288 | Ren *et al.*[47] |
| Al-BDC | 3.56 | 298 | Hu *et al.*[48] |
| $[Ni_3(HCOO)_6]$ | 6.02 | 298 | Hu *et al.*[48] |
| DDR | 6.1 | 298 | Krishna *et al.*[49] |

range of 0–100 kPa at 273.15 K. The order for the selectivity of equimolar $CH_4/N_2$ is as follows: Cu-BTC/CuO/CFP (0.30 : 0.13 : 0.57) > Cu-BTC/CuO/CFP (0.28 : 0.11 : 0.61) > Cu-BTC/CuO/CFP (0.09 : 0.21 : 0.70) under the same pressure. The effect of CuO content on the selectivity of $CH_4/N_2$ is non-monotonic. The selectivity of $CH_4/N_2$ first increases and then decreases with an increase in CuO content and the optimal CuO content is approximately 0.13 in the test samples. CuO and Cu-BTC exhibit a competitive relationship during the synthetic process. When the content of CuO is relatively low at 0.11, the growth of Cu-BTC crystallites is difficult to restrain. Thus, the



**Fig. 7** Selectivity of equimolar $CH_4/N_2$ mixture with different components.

number of Cu-BTC crystallites decreases, as shown in Fig. S5.† The amount of newly formed micropores as well as incomplete micropores, as shown in Fig. 5(c), decreases. The decrease in the number of micropores lowers the selectivity of $CH_4/N_2$. When the content of CuO is relatively high at 0.21, the amount of formed Cu-BTC crystals, which play a dominant role in the selectivity of $CH_4/N_2$, is reduced, and the newly formed and incomplete micropores also decrease. Thus, a lower selectivity
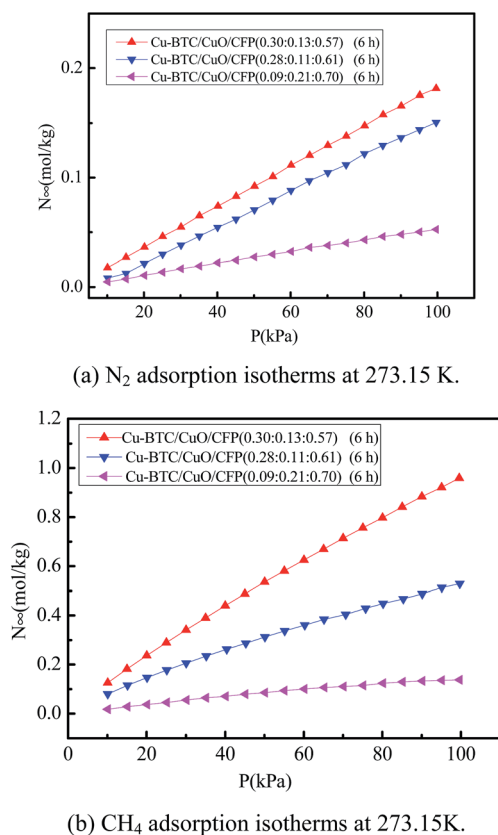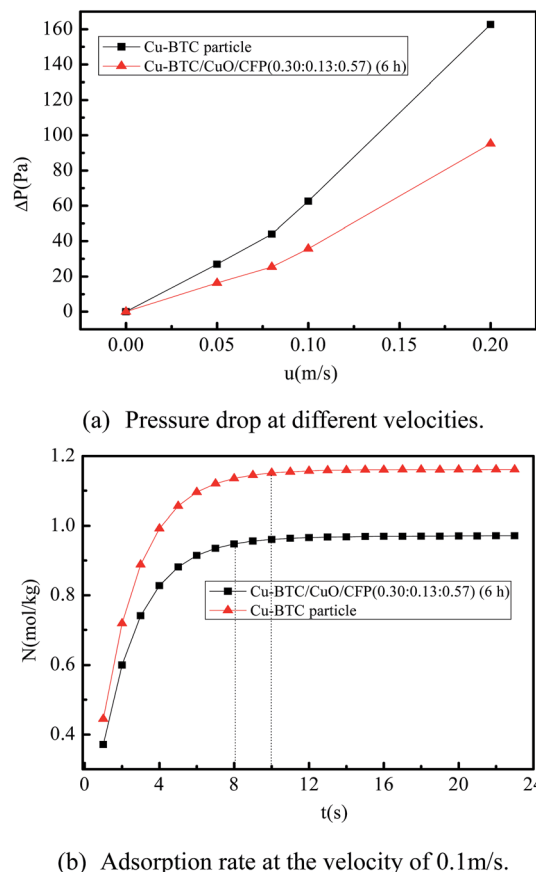


(a) N₂ adsorption isotherms at 273.15 K.



(b) CH₄ adsorption isotherms at 273.15K.

**Fig. 6** $N_2$ and $CH_4$ adsorption isotherms at 273.15 K.



(a) Pressure drop at different velocities.



(b) Adsorption rate at the velocity of 0.1m/s.

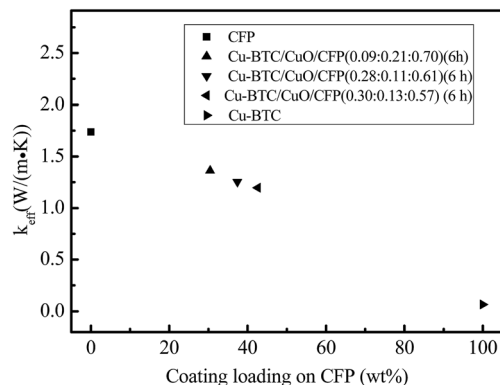**Fig. 8** Pressure drop and adsorption rate of Cu-BTC/CuO/CFP and Cu-BTC particles.

**Fig. 9** Effective thermal conductivity of different samples.

of equimolar $CH_4/N_2$ is obtained. For example, the selectivity of $CH_4/N_2$ in Cu-BTC/CuO/CFP (0.09 : 0.21 : 0.70) is even worse than that in pure Cu-BTC, as shown in Fig. 5(a). Therefore, a moderate optimal amount of CuO in Cu-BTC/CFP (0.30 : 0.13 : 0.57) was investigated. The moderate CuO not only contributes to the formation of an abundant amount of Cu-TBC crystals, but also provides new small micropores between Cu-BTC and CuO and CuO and CFP to easily adsorb $CH_4$.

### 4.3. The pressure drop and adsorption rate in the adsorption bed

The pressure drop is the key factor to determine energy consumption. Fig. 8(a) shows the comparison result for the pressure drop in the studied adsorption bed filled with Cu-BTC/CuO/CFP (0.30 : 0.13 : 0.57) (6 h) and pure Cu-BTC particles. The operating velocity was the range from 0 to 0.2 m s$^{-1}$. The pressure drop of the adsorption bed increased with increased velocity for the two filled materials. The pressure drop of Cu-BTC/CuO/CFP (0.30 : 0.13 : 0.57) (6 h) is 39.78–42.87% lower than that of the Cu-BTC particles. This phenomenon is caused by the higher porosity of Cu-BTC/CuO/CFP (0.78 in Table 2) compared to that of Cu-BTC particles (0.41 in Table 3). The adsorption rate is also a factor to determine the time approaching saturated adsorption. Fig. 8(b) shows the adsorption rate at different times at the typical velocity of 0.1 m s$^{-1}$. The time taken to reach saturation of adsorption in Cu-BTC/CuO/CFP (0.30 : 0.13 : 0.57) (6 h) is 20% (8 min) lower than that in the Cu-BTC particles because of the lower porosity of Cu-BTC/CuO/CFP.

### 4.4. The effective thermal conductivity and temperature response

Fig. 9 shows the effective thermal conductivity of CFP, Cu-BTC/CuO/CFP (0.09 : 0.21 : 0.70) (6 h), Cu-BTC/CuO/CFP
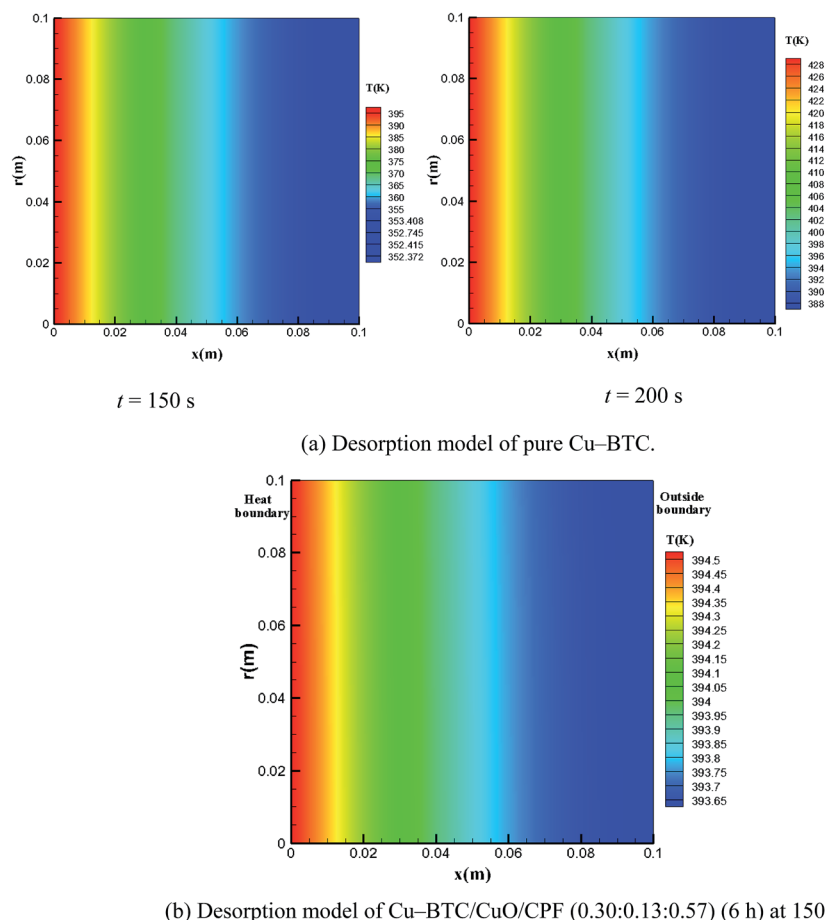


$t = 150$ s                    $t = 200$ s

(a) Desorption model of pure Cu–BTC.



(b) Desorption model of Cu–BTC/CuO/CPF (0.30:0.13:0.57) (6 h) at 150 s.

**Fig. 10** Temperature response of the desorption models.

(0.28 : 0.11 : 0.61) (6 h), Cu-BTC/CuO/CFP (0.30 : 0.13 : 0.57) (6 h), and Cu-BTC. CFP possesses the highest thermal conductivity of 1.738 W (m$^{-1}$ K$^{-1}$), whereas Cu-BTC has a lower effective thermal conductivity of 0.0678 W (m$^{-1}$ K$^{-1}$) because abundant micropores exist in the Cu-BTC crystals due to the coordination polymer. The effective thermal conductivity of Cu-BTC/CuO/CFP is mainly dependent on the contents of CFP and it decreases with an increase in Cu-BTC/CuO loading. Although the effective thermal conductivity of Cu-BTC/CuO/CFP (0.30 : 0.13 : 0.57) (6 h) is 87.8 percent lower than that of Cu-BTC/CuO/CFP (0.09 : 0.21 : 0.70) (6 h), it is still 17.64 times higher than that of the pure Cu-BTC.

Temperature uniformity and heat-up time, which can be significantly influenced by the effective thermal conductivity, are important index properties in the process of desorption. Fig. 10(a) shows the temperature distribution at different times (150 and 200 s) in the pure Cu-BTC powder adsorption bed in the process of desorption. Desorption conditions are required when the outside boundary surface temperature is above 373.15 K at the vacuum of 10$^{-5}$ kPa. The outside boundary surface temperature is only 352.4 K at 150 s and cannot meet the desorption requirement; thus, this requirement is satisfied at 200 s. In addition, the temperature in the pure Cu-BTC adsorption bed is inhomogeneous, with the temperature difference of 40.0 K between the two boundaries. Fig. 10(b) presents the temperature distribution in Cu-BTC/CuO/CFP (0.30 : 0.13 : 0.57) at 150 s. The outside boundary surface temperature can reach up to 393.65 K to satisfy the desorption requirement. The temperature uniformity also improved due to the enhanced thermal conductivity. The difference in the average surface temperature between the heating surface and outside boundary was less than 0.9 K.

## 5. Conclusion

A multi-level porous composite adsorbent, Cu-BTC/CuO/CFP (0.30 : 0.13 : 0.57), was synthesized at the synthesis time of 6 h. Although the amount of N$_2$ and CH$_4$ adsorption in Cu-BTC/CuO/CFP (0.30 : 0.13 : 0.57) (6 h) is between that of pure Cu-BTC and CFP, Cu-BTC/CuO/CFP (0.30 : 0.13 : 0.57) (6 h) exhibits the highest selectivity of CH$_4$/N$_2$ among the other Cu-BTC/CFP with the synthesis times of 3, 9, 18, and 24 h, and its selectivity is 2.15–2.65 times higher than that of pure Cu-BTC within the pressure range of 0–100 kPa at 273.15 K. This superior selectivity is attributed to the formation of small micropores between Cu-BTC and CuO and CuO and CFP. The pressure drop of Cu-BTC/CuO/CFP (0.30 : 0.13 : 0.57) (6 h) is 39.78–42.87% lower at the velocities ranging from 0 to 0.2 m s$^{-1}$ and the time taken to reach saturation of adsorption is also 20% lower than that in pure Cu-BTC particles at 0.1 m s$^{-1}$. The effective thermal conductivity of Cu-BTC/CuO/CFP (0.30 : 0.13 : 0.57) (6 h) is still 17.64 times higher than that of pure Cu-BTC powder. Thus, the temperature uniformity of the adsorption bed (150 s) is significantly improved and the desorption condition is conveniently satisfied compared with those of pure Cu-BTC.

## Acknowledgements

## References

1 C. M. Simon, J. Kim, D. A. Gomez-Gualdron, J. S. Camp, Y. G. Chung, R. L. Martin, R. Mercado, M. W. Deem, D. Gunter, M. Haranczyk, D. S. Sholl, R. Q. Snurr and B. Smit, The materials genome in action: identifying the performance limits for methane storage, *Energy Environ. Sci.*, 2015, **8**, 1190–1199.

2 H. Wu, W. Zhou and T. Yildirim, High-capacity methane storage in metal–organic frameworks M$_2$(dhtp): the important role of open metal sites, *J. Am. Chem. Soc.*, 2009, **131**, 4995–5000.

3 Q. Y. Yang and C. L. Zhong, Molecular simulation of carbon dioxide/methane/hydrogen mixture adsorption in metal–organic frameworks, *J. Phys. Chem. B*, 2006, **110**, 17776–17783.

4 A. Kertik, A. L. Khanb and I. F. J. Vankelecom, Mixed matrix membranes prepared from non-dried MOFs for CO$_2$/CH$_4$ separations, *RSC Adv.*, 2016, **6**, 114505–114512.

5 Y. Peng, V. Krungleviciute, I. Eryazici, J. T. Hupp, O. K. Farha and T. Yildirim, Methane storage in metal–organic frameworks: current records, surprise findings, and challenges, *J. Am. Chem. Soc.*, 2013, **135**, 11887–11894.

6 Z. Hulvey, B. Vlaisavljevich, J. A. Mason, E. Tsivion, T. P. Dougherty, E. D. Bloch, M. Head-Gordon, B. Smit, J. R. Long and C. M. Brown, Critical factors driving the high volumetric uptake of methane in Cu$_3$(btc)$_2$, *J. Am. Chem. Soc.*, 2015, **137**, 10816–10825.

7 L. Hamon, E. Jolimaître and G. D. Pirngruber, CO$_2$ and CH$_4$ separation by adsorption using Cu-BTC metal–organic framework, *Ind. Eng. Chem. Res.*, 2010, **49**, 7497–7503.

8 S. Liu, L. X. Sun, F. Xu, J. Zhang, C. L. Jiao, F. Li, Z. B. Li, S. Wang, Z. Q. Wang, X. Jiang, H. Y. Zhou, L. N. Yang and C. Schick, Nanosized Cu-MOFs induced by graphene oxide and enhanced gas storage capacity, *Energy Environ. Sci.*, 2013, **6**, 818–823.

9 A. Policicchio, Y. X. Zhao, Q. Zhong, R. G. Agostino and T. J. Bandosz, Cu-BTC/aminated graphite oxide composites as high-efficiency CO$_2$ capture media, *ACS Appl. Mater. Interfaces*, 2014, **6**, 101–108.

10 C. Petit, B. Mendoza and T. J. Bandosz, Reactive adsorption of ammonia on Cu-based MOF/graphene composites, *Langmuir*, 2010, **26**, 15302–15309.

11 F. Xu, Y. Yu, J. Yan, Q. B. Xia, H. H. Wang, J. Li and Z. Li, Ultrafast room temperature synthesis of GrO@HKUST-1 composites with high CO$_2$ adsorption capacity and CO$_2$/N$_2$ adsorption selectivity, *Chem. Eng. J.*, 2016, **303**, 231–237.

12 H. Wang, Z. G. Qu, W. Zhang and L. Q. Zhang, A multi-scale porous composite adsorbent with copper benzene-1,3,5-tricarboxylate coating on copper foam, *RSC Adv.*, 2016, **6**, 52888–52897.

13 B. L. Huang, Z. Ni, A. Millward, A. J. H. McGaughey, C. Uher, M. Kaviany and O. Yaghi, Thermal conductivity of a metal–organic framework (MOF-5): part II measurement, *Int. J. Heat Mass Transfer*, 2007, **50**, 405–411.

14 H. Wang, Z. G. Qu, W. Zhang, Q. N. Yu and Y. L. He, Experimental and numerical study of $CO_2$ adsorption on copper benzene-1,3,5-tricarboxylate (Cu-BTC) metal organic framework, *Int. J. Heat Mass Transfer*, 2016, **92**, 859–863.

15 J. J. Purewal, D. Liu, J. Yang, A. Sudik, D. J. Siegel, S. Maurer and U. Müler, Increased volumetric hydrogen uptake of MOF-5 by powder densification, *Int. J. Hydrogen Energy*, 2012, **37**, 2723–2727.

16 V. Radhakrishnan and P. Haridoss, Differences in structure and property of carbon paper and carbon cloth diffusion media and their impact on proton exchange membrane fuel cell flow field design, *Mater. Des.*, 2011, **32**, 861–868.

17 X. Q. Zhang, X. Y. Fan, C. Yan, H. Z. Li, Y. D. Zhu, X. T. Li and L. P. Yu, Interfacial microstructure and properties of carbon fiber composites modified with graphene oxide, *ACS Appl. Mater. Interfaces*, 2012, **4**, 1543–1552.

18 B. Silva, L. Solomon, A. M. Ribeiro, U. H. Lee, Y. K. Hwang, J. S. Chang, J. M. Loureiro and A. E. Rodrigues, $H_2$ purification by pressure swing adsorption using Cu-BTC, *Sep. Purif. Technol.*, 2013, **118**, 744–756.

19 J. Liu, J. Tian, P. K. Thallapally and B. P. Mcgrail, Selective $CO_2$ capture from flue gas using metal–organic frameworks – a fixed bed study, *J. Phys. Chem. C*, 2012, **116**, 9575–9581.

20 J. A. Wurzbacher, C. Gebald, S. Brunner and A. Steinfeld, Heat and mass transfer of temperature-vacuum swing desorption for $CO_2$ capture from air, *Chem. Eng. J.*, 2016, **283**, 1329–1338.

21 G. Majano and J. Pérez-Ramírez, Scalable room-temperature conversion of copper(II) hydroxide in HKUST-1 ($Cu_3$(btc)$_2$), *Adv. Mater.*, 2013, **25**, 1052–1057.

22 V. H. Jaggi and H. R. Oswald, Die kristallstruktur des kupferhydroxids $Cu(OH)_2$, *Acta Crystallogr.*, 1961, **14**, 1041.

23 D. A. Svintsitskiy, T. Y. Kardash, O. A. Stonkus, E. M. Slavinskaya, A. I. Stadnichenko, S. V. Koscheev, A. P. Chupakhin and A. I. Boronin, In situ XRD, XPS, TEM, and TPR study of highly active in CO oxidation CuO nanopowders, *J. Phys. Chem. C*, 2013, **117**, 14588–14599.

24 S. S. Y. Chui, S. M. F. Lo and J. P. H. Charmant, A chemically functionalizable nanoporous material $[Cu_3(TMA)_2(H_2O)_3]_n$, *Science*, 1999, **19**, 1148–1150.

25 Y. X. Zhao, M. Seredych, Q. Zhong and T. J. Bandosz, Superior performance of copper based MOF and aminated graphite oxide composites as $CO_2$ adsorbents at room temperature, *ACS Appl. Mater. Interfaces*, 2013, **5**, 4951–4959.

26 H. H. Chen, H. P. Zhang and Y. Yan, Preparation and characterization of a novel gradient porous ZSM-5 zeolite membrane/PSSF composite and its application for toluene adsorption, *Chem. Eng. J.*, 2012, **209**, 372–378.

27 S. W. Finefrock, Y. Wang, J. B. Ferguson, J. V. Ward, H. Y. Fang, J. E. Pfuger, D. S. Dudis, X. L. Ruan and Y. Wu, Measurement of thermal conductivity of PbTe nanocrystal coated glass fibers by the 3ω method, *Nano Lett.*, 2013, **13**, 5006–5012.

28 M. G. Plaza, A. M. Ribeiro, A. Ferreira, J. C. Santos, U. H. Lee, J. S. Chang, J. M. Loureiro and A. E. Rodrigues, Propylene/propane separation by vacuum swing adsorption using Cu-BTC spheres, *Sep. Purif. Technol.*, 2012, **90**, 109–119.

29 J. T. Gostick, M. W. Fowler, M. D. Pritzker, M. A. Ioannidis and L. M. Behra, In-plane and through-plane gas permeability of carbon fiber electrode backing layers, *J. Power Sources*, 2006, **162**, 228–238.

30 D. L. Sun, Z. G. Qu, Y. L. He and W. Q. Tao, An efficient segregated algorithm for incompressible fluid flow and heat transfer problems-IDEAL (Inner Doubly Iterative Efficient Algorithm for Linked Equations) part I: mathematical formulation and solution procedure, *Numer. Heat Transfer, Part B*, 2008, **53**, 1–17.

31 T. Van Heest, S. L. Teich-McGoldrick, J. A. Greathouse, M. D. Allendorf and D. S. Sholl, Identification of metal–organic framework materials for adsorption separation of rare gases: applicability of ideal adsorbed solution theory (IAST) and effects of inaccessible framework regions, *J. Phys. Chem. C*, 2012, **116**, 13183–13195.

32 W. Huang, X. Zhou, Q. Xia, J. Peng, H. Wang and Z. Li, Preparation and adsorption performance of GrO@Cu-BTC for separation of $CO_2/CH_4$, *Ind. Eng. Chem. Res.*, 2014, **53**, 11176–11184.

33 I. Langmuir, The adsorption of gases on plane surface of glass mica and platinum, *J. Am. Chem. Soc.*, 1918, **40**, 1361–1403.

34 S. R. Caskey, A. G. Wong-Foy and A. J. Matzger, Dramatic tuning of carbon uptake via metak substitution in a coordination polymer with cylindrical pores, *J. Am. Chem. Soc.*, 2008, **130**, 10870–10871.

35 Y. Wang and M. D. LeVan, Adsorption equilibrium of carbon dioxide and water vapor on zeolites 5A and 13X and silica gel: pure components, *J. Chem. Eng. Data*, 2009, **54**, 2839–2844.

36 Z. G. Qu, H. Wang, W. Zhang, L. Zhou and Y. X. Chang, Experimental verification of $CO_2$ adsorption on Ni/DOBDC using a genetic algorithm-back-propagation neural network model, *Ind. Eng. Chem. Res.*, 2014, **53**, 12044–12053.

37 J. Li, G. P. Yang, S. L. Wei, R. C. Gao, N. N. Bai and Y. Y. Wang, Two microporous metal–organic frameworks with suitable pore size displaying the high $CO_2/CH_4$ selectivity, *Cryst. Growth Des.*, 2015, **15**, 5382–5387.

38 D. Kim and H. Lee, Hydrophilic pore-blocked metal–organic frameworks: a simple route to highly selective $CH_4/N_2$ separation, *RSC Adv.*, 2015, **5**, 2749–2755.

39 L. Zhao, Q. Yang, Q. Ma, C. Zhong, J. Mi and D. Liu, A force field for dynamic Cu-BTC metal–organic framework, *J. Mol. Model.*, 2011, **17**, 227–234.

40 D. Nazarian, J. S. Camp, Y. C. G. Chung, R. Q. Snurr and D. S. Sholl, Large-scale refinement of metal–organic framework structures using density functional theory, *Chem. Mater.*, 2016, DOI: 10.1021/acs.chemmater.6b04226.

41 F. Salles, A. Ghoufi, G. Maurin, R. G. Bell, C. Mellot-Draznieks and G. Férey, Simulations of breathing MOFs: structural transformations of MIL-53 (Cr) upon thermal

activation and $CO_2$ adsorption, *Angew. Chem.*, 2008, **120**, 8615–8619.

42 X. Zhou, W. Huang, J. Miao, Q. Xia, Z. Zhang, H. H. Wang and Z. Li, Enhanced separation performance of a novel composite material GrO@MIL-101 for $CO_2/CH_4$ binary mixture, *Chem. Eng. J.*, 2015, **266**, 818–823.

43 O. Shekhah, H. Wang, S. Kowarik, F. Schreiber, M. Paulus, M. Tolan, C. Sternemann, F. Evers, D. Zacher, R. A. Fischer and C. Wöll, Step-by-step route for the synthesis of metal–organic frameworks, *J. Am. Chem. Soc.*, 2007, **129**, 15118–15119.

44 Y. Cai, A. R. Kulkarni, Y. G. Huang, D. S. Sholl and K. S. Walton, Control of metal–organic framework crystal topology by ligand functionalization: functionalized HKUST-1 derivatives, *Cryst. Growth Des.*, 2014, **14**, 6122–6128.

45 B. Liu and B. Smit, Molecular simulation studies of separation of $CO_2/N_2$, $CO_2/CH_4$, and $CH_4/N_2$ by ZIFs, *J. Phys. Chem. C*, 2010, **114**, 8515–8522.

46 B. Liu and B. Smit, Comparative molecular simulation study of $CO_2/N_2$ and $CH_4/N_2$ separation in zeolites and metal–organic frameworks, *Langmuir*, 2009, **25**, 5918–5926.

47 X. Y. Ren, T. J. Sun, J. L. Huab and S. D. Wang, Synthesis optimization of the ultra-microporous $[Ni_3(HCOO)_6]$ framework to improve its $CH_4/N_2$ separation selectivity, *RSC Adv.*, 2014, **4**, 42326–42336.

48 J. L. Hu, T. J. Sun, X. W. Liu, Y. Guo and S. D. Wang, Separation of $CH_4/N_2$ mixtures in metal–organic frameworks with 1D micro-channels, *RSC Adv.*, 2016, **6**, 64039–64046.

49 R. Krishna, M. Jasper and V. Baten, Comment on comparative molecular simulation study of $CO_2/N_2$ and $CH_4/N_2$ separationin zeolites and metal–organic frameworks, *Langmuir*, 2010, **26**, 2975–2978.